PAPER

Check for updates

Probing the activity of transition metal M and heteroatom N_4 co-doped in vacancy fullerene ($M-N_4-C_{64}$, M = Fe, Co, and Ni) towards the oxygen reduction reaction by density functional theory

Siwei Yang, Chaoyu Zhao, [ID] Ruxin Qu, Yaxuan Cheng, Huiling Liu [ID]* and Xuri Huang*

In this study, a novel type oxygen reduction reaction (ORR) electrocatalyst is explored using density functional theory (DFT); the catalyst consists of transition metal M and heteroatom N_4 co-doped in vacancy fullerene ($M-N_4-C_{64}$, M = Fe, Co, and Ni). Mulliken charge analysis shows that the metal center is the reaction site of ORR. PDOS analysis indicates that in $M-N_4-C_{64}$, the interaction between $Fe-N_4-C_{64}$ and the adsorbate is the strongest, followed by $Co-N_4-C_{64}$ and $Ni-N_4-C_{64}$. This is consistent with the calculated adsorption energies. By analyzing and comparing the adsorption energies of ORR intermediates and activation energies and reaction energies of all elemental reactions in $M-N_4-C_{64}$ (M = Fe, Co, and Ni), two favorable ORR electrocatalysts, $Fe-N_4-C_{64}$ and $Co-N_4-C_{64}$, are selected. Both exhibited conduction through the more efficient $4e^-$ reduction pathway. Moreover, PES diagrams indicate that the whole reaction energy variation in the favorable ORR pathways of $Fe-N_4-C_{64}$ and $Co-N_4-C_{64}$ is degressive, which is conducive to positive-going reactions. This study offers worthwhile information for the improvement of cathode materials for fuel cells.

1. Introduction

With the expansion of industrialization and urbanization, environmental pollution and energy consumption are being increasingly aggravated. Fuel cells (FCs) have become the most promising power generation technology, with the characteristics of sustainable, pollution-free and wide-ranging fuel sources.[1–4] The oxygen reduction reaction (ORR) is carried out in the cathode through $2e^-$ and $4e^-$ pathways.[5,6] The $4e^-$ pathway directly reduces O_2 to H_2O and has high energy conversion efficiency; hence, it is the preferred pathway for FCs.[7,8] However, the $2e^-$ pathway (the less efficient pathway involving the formation of H_2O_2 as an intermediate) and slow kinetics on the cathode hinder the power generation efficiency of FCs.[9–11] In addition, Pt-based catalysts, which are considered to be highly efficient,[12,13] have limited commercial applications in FCs due to their high cost.[14,15] Therefore, it is urgent to exploit high-performance and inexpensive ORR electrocatalysts to substitute the expensive Pt-based catalysts on the market.

Because single-atom catalysts (SACs) have different activity, selectivity and stability from traditional nanocatalysts,[16,17] they are proposed to exhibit remarkable behavior in various energy transformation reactions, such as HER,[18,19] CO_2RR[20,21] and ORR.[22,23] Moreover, the realization of single-atom dispersion of SACs usually requires a suitable substrate and dopant.[24] Fullerenes are cage structures in which carbon atoms form a conjugated system through sp^2 hybridization.[25] As non-metallic materials with a wide range of sources, fullerenes have demonstrated excellent performance including biological applications,[26] energy storage,[27] thermoelectric materials,[28] and optoelectronic devices.[29] In addition, as a result of the curvature and pentagon defects of fullerenes,[30,31] they can be used as promising candidates for electrocatalytic reactions. Vinu *et al.* investigated a polymeric mesoporous fullerene C_{60} material prepared at 130 °C (MFC_{60}-130), which showed effective ORR behavior benefiting from its specific surface area of 680 $m^2\ g^{-1}$ and steady and conductive C_{60} reticulation.[32] Subsequently, Vinu *et al.* continued to report mesoporous fullerene C_{70} materials, which were endowed with good mesoporous framework, excellent conductivity and connectivity; further, materials exhibited good ORR performance.[33] However, it is necessary to improve their electrocatalytic properties for practical applications.

Heteroatom doping is an effectual way to regulate the electronic and conductive properties of fullerenes and enhance their electrocatalytic behavior.[34,35] Chen *et al.* discovered that

Laboratory of Theoretical and Computational Chemistry, Institute of Theoretical Chemistry, Jilin University, Liutiao Road 2, Changchun 130023, China. E-mail: huiling@jlu.edu.cn; huangxr@jlu.edu.cn

nitrogen-doped fullerenes showed higher ORR properties than pure fullerenes.[36] Wang *et al.* also reported that nitrogen-doped C_{60} cages ($C_{59}N$) exhibited superior ORR electrocatalytic activity to other heteroatom-doped C_{60} cages,[37] which was further experimentally proved by Gao *et al.*[35]

Furthermore, to facilitate the embedding of metal atoms, introducing vacancies in the substrate can change the coordination environment and electronic structure around the vacancies; thus, under-coordinated sites can act as bait and vacancies can act as traps to trap metal atoms.[38,39] The co-doping of transition metal atoms and heteroatoms on vacant carbon materials has been widely studied both experimentally and theoretically. Fe-porphyrin-like carbon nanotubes synthesized by Lee *et al.* showed excellent oxygen reduction activity due to the characteristics of the Fe–N₄ structure.[40] Fei *et al.* found that the composite material obtained by embedding individual Ni atoms into the double vacancies of an N-doped graphene lattice displayed higher oxygen evolution reaction (OER) activity and stability.[41] Chen *et al.* embedded individual iron atoms into N-pore carbon through the thermolysis approach of cage-encapsulated precursors, and the composite exhibited remarkable ORR properties and satisfactory methanol tolerance.[42] Recently, Wang *et al.* reported synthesized Fe-anchored graphite carbonitride, which was used in CO₂RR to improve the selectivity of CO and realize the high-efficiency transformation of CO_2 due to the Fe–N₄ sites in the composite.[43] Theoretically, many studies have illuminated that metal–N₄-vacancy carbon materials have attractive performance as cathode materials for FCs.[44–47] Significantly, Brindaban Modak *et al.* found that transition metal-modified porous fullerene $C_{24}N_{24}$ can serve as an oxygen reduction electrocatalyst and carry out a more effectual $4e^-$ reduction mechanism.[48] These reports led us to wonder whether transition metal and heteroatom N could be co-doped in vacancy fullerenes as effective electrocatalysts for ORR. However, related reports are rare. Therefore, we systematically studied all possible intermediate steps involved in the ORR process of co-doping transition metal M and heteroatom N₄ in vacancy fullerene (M–N₄–C₆₄, M = Fe, Co, and Ni). The promising ORR electrocatalysts were selected and the corresponding favorable ORR pathways were determined. This work offers worthwhile information for the improvement of cathode materials for FCs.

2. Computational methods

All calculations were carried out using the spin-polarized DFT implemented in Materials Studio DMol³ code.[36,49] The generalized gradient approximation of the Perdew–Burke–Ernzerhof functional (GGA + PBE),[48,50] together with all electrons and the double numerical basis set (DNP), was adopted throughout all calculations. To improve computational performance, the self-consistent field (SCF) was converged to 10^{-6} Ha and the smearing was set to 0.005 Ha. The convergence tolerance was 2×10^{-5} Ha for the energy change, 0.004 Ha Å⁻¹ for the max force and 0.005 Å for the max displacement. The Grimme method for DFT-D correction was used to describe the van der Waals

interactions. The energy difference between the transition state and the reactant was the activation barrier (E_{act}).

The formation energy (E_f) of M–N₄ co-doped in vacancy fullerene was calculated as follows:

$$E_f = E_{M-N_4-C_{64}} + 6\mu_C - (E_{fullerene} + 4\mu_N + E_M)$$

where $E_{M-N_4-C_{64}}$ and $E_{fullerene}$ are the energies of the optimized M–N₄–C₆₄ and perfect fullerene C_{70}, correspondingly. μ_C and μ_N are the chemical potentials of carbon and nitrogen atoms, which were obtained by the total energy per C atom in perfect fullerene C_{70} and one half of an N_2 gas molecule, correspondingly. E_M is the energy of the individual metal atom.

The adsorption energy (E_{ads}) was calculated as follows:

$$E_{ads} = E_{adsorbate@M-N_4-C_{64}} - E_{M-N_4-C_{64}} - E_{adsorbate}$$

where $E_{adsorbate@M-N_4-C_{64}}$, $E_{M-N_4-C_{64}}$ and $E_{adsorbate}$ refer to the energies of M–N₄–C₆₄ (M = Fe, Co, and Ni) with the adsorbate, individual M–N₄–C₆₄ and the individual adsorbate, correspondingly.

3. Results and discussion

3.1 Configuration and properties of M–N₄–C₆₄

To embed M-N₄ in fullerene, as Fig. 1a shows, the no. 1 and 2 carbon atoms in the optimized fullerene C_{70} were removed. Then, four nitrogen atoms were utilized to substitute the no. 3, 4, 5 and 6 carbon atoms, which had insufficient coordination. Finally, the metal atom was incorporated in the center of the vacancy. We calculated the different multiplicities of M–N₄–C₆₄ (M = Fe, Co, and Ni) to obtain the most stable energies. The results show that the most stable states for Fe–N₄–C₆₄, Co–N₄–
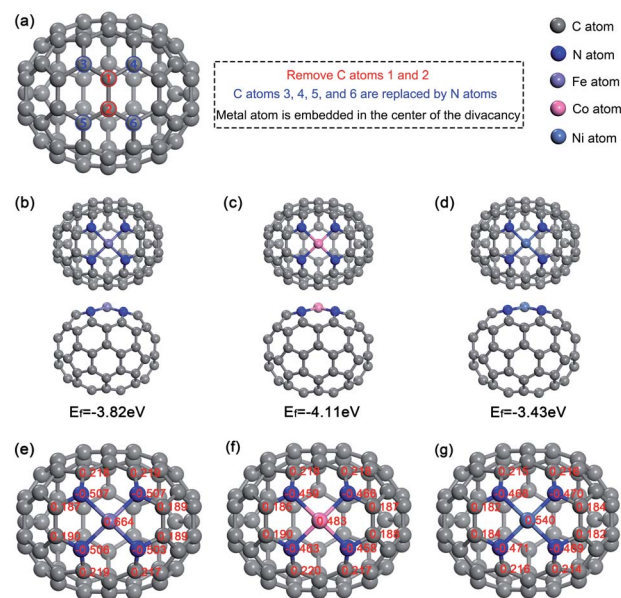

Fig. 1 The optimized configurations of (a) C_{70}, (b) Fe–N₄–C₆₄, (c) Co–N₄–C₆₄ and (d) Ni–N₄–C₆₄. Charge distributions on (e) Fe–N₄–C₆₄, (f) Co–N₄–C₆₄ and (g) Ni–N₄–C₆₄.

C_{64}, and Ni–N_4–C_{64} are triplet, doublet, and singlet, correspondingly. The oxygen molecule is a triplet in our research system. The stable configurations of Fe–N_4–C_{64}, Co–N_4–C_{64} and Ni–N_4–C_{64} were optimized (see Fig. 1b–d), and the formation energies (E_f) of the three configurations were calculated as −3.82, −4.11, and −3.43 eV, correspondingly. This finding demonstrates that Fe–N_4–C_{64}, Co–N_4–C_{64} and Ni–N_4–C_{64} are thermodynamically stable. In addition, as can be seen from the Mulliken charges in Fig. 1e–g, nitrogen atoms in M–N_4–C_{64} (M = Fe, Co, and Ni) show negative charge density, while the adjacent carbon atoms show positive charge density. This is caused by the fact that the electronegativity of N atoms is greater than that of C atoms. This porphyrin-like structure can stably fix M–N_4 embedded on C_{64}. The Mulliken charges of the Fe, Co and Ni atoms were calculated as 0.664, 0.483 and 0.540|e|, correspondingly. Because a positively charged site is more advantageous for O_2 adsorption, the metal center was chosen as the reaction site for ORR. On the other hand, it was found that in the Fe–N_4–C_{64} system, the electron transfer from the metal center to N_4–C_{64} is the largest.

3.2 Electronic structure of M–N_4–C_{64}

The calculated DOS (see Fig. 2a) display that the band gaps of Fe–N_4–C_{64}, Co–N_4–C_{64} and Ni–N_4–C_{64} are all zero, which reveals that they have the potential to be ORR electrocatalysts due to their excellent electrical conductivity.

The calculated PDOS (see Fig. 2b–d) display that the C-2p and N-2p orbitals in M–N_4–C_{64} (M = Fe, Co, and Ni) exhibit strong resonance regions below the Fermi level, which indicates that the interaction between C and N is very strong. Meanwhile, the PDOS display that in M–N_4–C_{64}, the Co-3d orbital contribution is the most average below the Fermi level, followed by Fe-3d and finally Ni-3d, which is consistent with stability of the
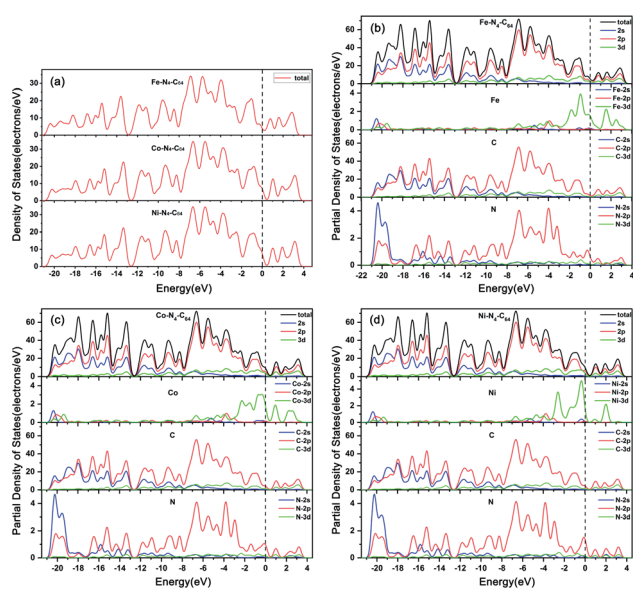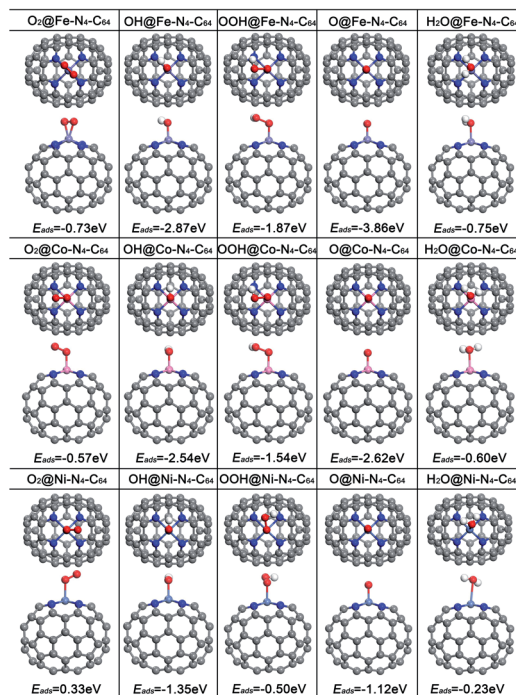

Fig. 3 The optimized configurations of the adsorption of O_2, OH, OOH, O and H_2O on Fe–N_4–C_{64}, Co–N_4–C_{64} and Ni–N_4–C_{64}.

calculated E_f for M–N_4–C_{64}. In addition, the calculated d-band centers in the range of −8.0 eV–4 eV are −1.24 eV for Fe–N_4–C_{64}, −1.33 eV for Co–N_4–C_{64} and −1.61 eV for Ni–N_4–C_{64}, which demonstrates that the interaction between Fe–N_4–C_{64} and the adsorbate is the strongest among the three, followed by Co–N_4–C_{64} and finally Ni–N_4–C_{64}. This is attributable to the fact that the upward shift of the d-band center to the Fermi level will arouse the upward shift of the antibonding orbitals; thus, they are

Fig. 2 (a) The densities of states for Fe–N_4–C_{64}, Co–N_4–C_{64} and Ni–N_4–C_{64}. The partial densities of states for (b) Fe–N_4–C_{64}, (c) Co–N_4–C_{64} and (d) Ni–N_4–C_{64}.

Table 1 Activation barriers (E_{act}), reaction energies (ΔE) and virtual frequencies (V_{freq}) of the basic reaction steps for the ORR on M–N_4–C_{64} (M = Fe, Co, and Ni)

| Catalysts	Reaction steps	E_{act} (eV)	ΔE (eV)	V_{freq} (cm^{-1})
Fe–N_4–C_{64}	*O_2 → *O + *O	2.25	0.40	i439
	*O_2 + *H → *OOH	0.06	−0.97	i1514
	*OOH + *H → *H_2O_2	2.77	−0.31	i1026
	*OOH + *H → *O + *H_2O	0.32	−1.21	i1355
	*O + *H → *OH	0.34	−1.35	i1298
	*OH + *H → *H_2O	0.47	−0.60	i1426
Co–N_4–C_{64}	*O_2 → *O + *O	2.93	1.46	i561
	*O_2 + *H → *OOH	0.13	−0.69	i981
	*OOH + *H → *H_2O_2	0.80	−0.46	i1469
	*H_2O_2 → *O + *H_2O	0.33	−0.23	i627
	*OOH + *H → *O + *H_2O	0.78	−0.41	i768
	*O + *H → *OH	0.04	−2.10	i918
	*OH + *H → *H_2O	0.22	−0.86	i1467
Ni–N_4–C_{64}	*O_2 + *H → *OOH	0.08	−0.36	i1102
	*OOH + *H → *O + *H_2O	0.68	0.21	i454
	*O + *H → *OH	3.25	−2.43	i468
	*OH + *H → *H_2O	2.97	−1.93	i767
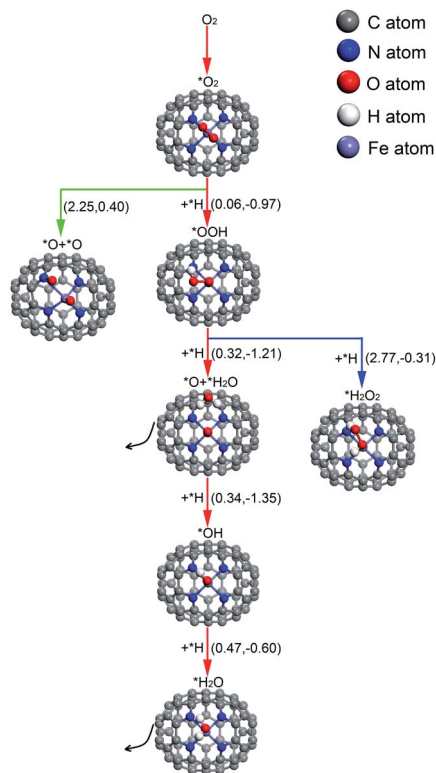
Fig. 4 The conceivable ORR pathways on Fe−N$_4$−C$_{64}$. The value on the left in parentheses is the activation energy and the value on the right is the reaction energy (in eV). * indicates adsorbed species.

harder to fill, and in turn, the interaction between the catalyst and adsorbates is stronger.

3.3 The adsorption of ORR species on M−N$_4$−C$_{64}$

The adsorption of ORR species plays a formative role in the study of the ORR mechanism and electrocatalytic activity. For comparison, Fig. 3 exhibits the optimized adsorption configurations of the ORR species (O$_2$, OH, OOH, O and H$_2$O) on M−N$_4$−C$_{64}$ (M = Fe, Co, and Ni), and the corresponding adsorption energies (E_{ads}) were calculated. The results manifest that E_{ads} weakens in this sequence: Fe−N$_4$−C$_{64}$ > Co−N$_4$−C$_{64}$ > Ni−N$_4$−C$_{64}$, which is in line with the results of the PDOS analysis. The electrocatalytic capability of the catalyst can be exhibited visually by the chemisorption of O$_2$ molecule on the substrate as the preliminary stage of ORR. The O$_2$ molecule is stably adsorbed on the Fe center of Fe−N$_4$−C$_{64}$ by side-on configuration, and the E_{ads} was calculated as −0.73 eV. After adsorption, d_{O-O} is 1.345 Å (d_{A-B} represents the distance between A and B), which is increased compared with that of the individual O$_2$ molecule (1.225 Å). The O$_2$ is stably adsorbed on the Co center of Co−N$_4$−C$_{64}$ by end-on configuration, and the E_{ads} was calculated as −0.57 eV. After adsorption, d_{O-O} is 1.270 Å, which is slightly larger than that of the individual O$_2$ molecule (1.225 Å). However, in the Ni−N$_4$−C$_{64}$ system, the calculated E_{ads} of the O$_2$ is 0.33 eV, and the positive value of E_{ads} indicates that it is unbound relative to the separated O$_2$. This indicates that the ORR behavior of Ni−N$_4$−C$_{64}$ is disadvantageous. Atomic O is adsorbed on Fe−N$_4$−C$_{64}$ and Co−N$_4$−C$_{64}$ with the strongest E_{ads}
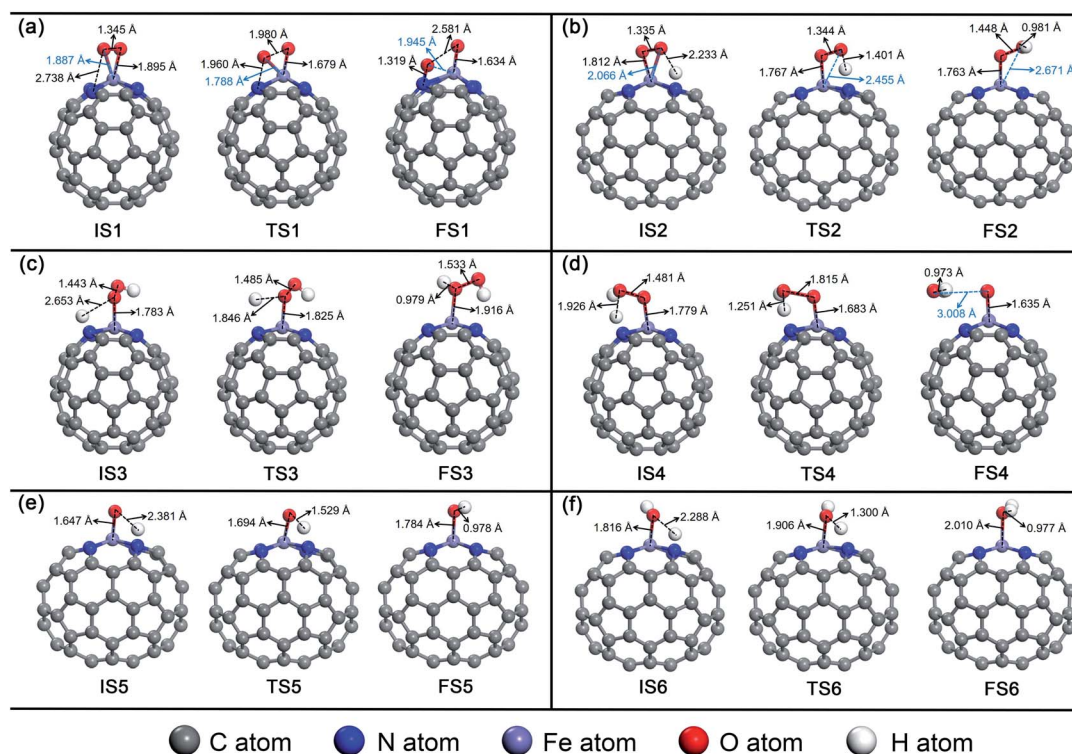
Fig. 5 The detailed process of the ORR on Fe−N$_4$−C$_{64}$. (a) *O$_2$ → *O + *O, (b) *O$_2$ + *H → *OOH, (c) *OOH + *H → *H$_2$O$_2$, (d) *OOH + *H → *O + *H$_2$O, (e) *O + *H → *OH, and (f) *OH + *H → *H$_2$O.

values of -3.86 and -2.62 eV, correspondingly. The $E_{ads}(OH)$ for M–N_4–C_{64} (M = Fe, Co, and Ni) is larger than that of E_{ads}(-OOH). Furthermore, for the ORR product H_2O, the E_{ads} is -0.75 eV for Fe–N_4–C_{64}, -0.60 eV for Co–N_4–C_{64} and -0.23 eV for Ni–N_4–C_{64}. These weak E_{ads} values are close to the solvation energy ($\sim$$-0.40$ eV) of massive H_2O.[45,51] Therefore, once H_2O is formed, it can be effortlessly separated from M–N_4–C_{64}.

3.4 ORR mechanisms on M–N_4–C_{64}

The ORR mechanisms on M–N_4–C_{64} (M = Fe, Co, and Ni) are complicated. To prove that the three catalysts can serve as effective ORR electrocatalysts, we will systematically study the ORR mechanisms of the three systems in the following sections. The activation barriers (E_{act}), reaction energies (ΔE) and virtual frequencies (V_{freq}) of all the ORR basic reaction steps involved in M–N_4–C_{64} (M = Fe, Co, and Ni) are listed in Table 1.

3.4.1 ORR mechanisms on Fe–N_4–C_{64}. The ORR mechanisms on Fe–N_4–C_{64} were studied, and all conceivable pathways are placed in Fig. 4, where the red line pathway represents the optimal summarized ORR mechanism for Fe–N_4–C_{64}. The details of the ORR on Fe–N_4–C_{64} will be discussed next.

For O_2 chemisorbed on Fe–N_4–C_{64}, there are two conceivable pathways: dissociation (*O_2 → *O + *O) and hydrogenation (*O_2 + *H → *OOH) (* indicates adsorbed species). For *O_2 → *O + *O, this reaction requires an endothermic reaction energy of 0.40 eV and is accompanied by a high activation barrier (E_{act}) of 2.25 eV. This indicates that the stage of *O_2 → *O + *O on Fe–N_4–C_{64} is disadvantageous in thermodynamics and kinetics. The dissociation details are presented in Fig. 5a. Conversely, the hydrogenation of *O_2 to *OOH is more feasible because for *O_2 + *H → *OOH, this reaction has an exothermic reaction energy of 0.97 eV. Moreover, this process is accompanied by an extremely low E_{act} of 0.06 eV, which is obviously lower than the E_{ads} of *O_2 (-0.73 eV) on Fe–N_4–C_{64}. The virtual frequency (V_{freq}) of $i1514$ cm^{-1} in the transition state TS2 exactly shows the formation of the intermediate *OOH. The hydrogenation details (see Fig. 5b) indicate that d_{O-H} decreases from 2.233 Å in IS2 to 1.401 Å in TS2 and to 0.981 Å in FS2. Meanwhile, the distance between the atomic O which is attacked by the atomic H and the Fe atom extends from 2.066 Å in IS2 to 2.455 Å in TS2 and to 2.671 Å in FS2, and the *OOH intermediate in FS2 is adsorbed on the Fe site by end-on configuration. Furthermore, d_{O-O} extends from 1.335 Å in IS2 to 1.448 Å in FS2, which indicates that the interaction between the two O atoms is weakened and subsequent reactions will occur.

For the formed *OOH, there are two conceivable hydrogenation pathways: the *H attacks the O atom that bonds to Fe to afford *H_2O_2 (*OOH + *H → *H_2O_2), or *H attacks the hydroxyl oxygen in *OOH to afford *O and *H_2O (*OOH + *H → *O + *H_2O). For *OOH + *H → *H_2O_2, this reaction is accompanied by an insurmountable E_{act} of 2.77 eV, which manifests that the $2e^-$ pathway to generate *H_2O_2 on Fe–N_4–C_{64} is kinetically infeasible. This hydrogenation details are described in Fig. 5c. Conversely, the reaction *OOH + *H → *O + *H_2O releases 1.21 eV of energy with a low E_{act} of 0.32 eV, which is more feasible under the support of thermodynamics and kinetics.

Moreover, the energy required for this stage is notably lower than the E_{ads} of *OOH (-1.87 eV) on Fe–N_4–C_{64}. The V_{freq} of $i1355$ cm^{-1} in TS4 exactly exhibits the formation of *H_2O, and the formed *H_2O can be effortlessly detached from the Fe–N_4–C_{64} surface, which only requires a very low energy of 0.27 eV. The hydrogenation details (see Fig. 5d) indicate that d_{Fe-O} shortens from 1.779 Å in IS4 to 1.635 Å in FS4 and d_{O-O} increases from 1.481 Å in IS4 to 3.008 Å in FS4. This indicates that the interaction between Fe–O is strengthened and the O–O bond is broken.

Finally, the atomic O remaining on Fe experiences continuous hydrogenation to afford the second *H_2O: *O + *H → *OH and *OH + *H → *H_2O. The former reaction has a large exothermic reaction energy of 1.35 eV. Moreover, this process is accompanied by a low E_{act} of 0.34 eV, which is significantly lower than the E_{ads} of *O (-3.86 eV) on Fe–N_4–C_{64}. The hydrogenation details (see Fig. 5e) indicate that d_{O-H} diminishes from 2.381 Å in IS5 to 0.978 Å in FS5. Moreover, in TS5, the Fe–O bond is tilted to promote the formation of *OH. The d_{Fe-O} length increases from 1.647 Å in IS5 to 1.784 Å in FS5, which manifests that the interaction between Fe–O is weakened with the formation of *OH. Then, the *OH remaining on Fe experiences the succeeding hydrogenation: *OH + *H → *H_2O. This stage has an exothermic reaction energy of 0.60 eV. Moreover,

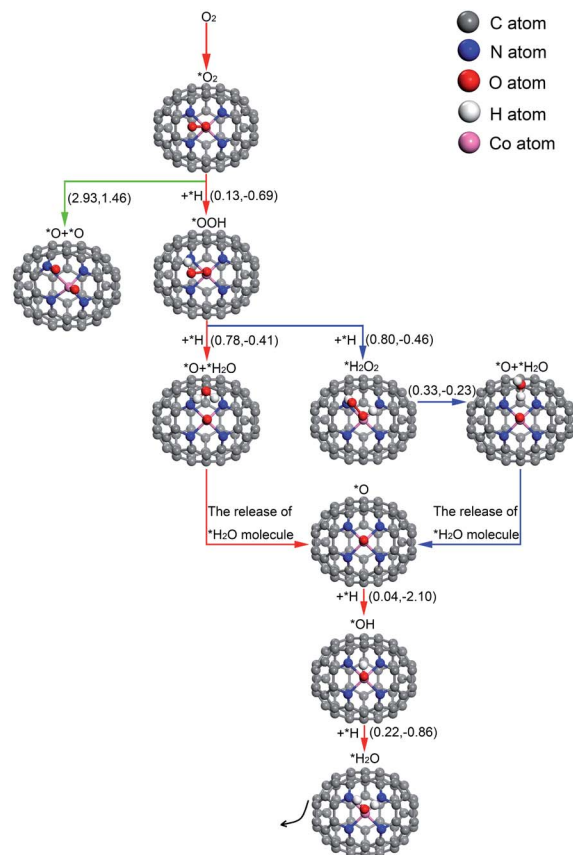**Fig. 6** The conceivable ORR pathways on Co–N_4–C_{64}. The value on the left in parentheses is the activation energy and the value on the right is the reaction energy (in eV). * means adsorbed species.

this process is accompanied by a low E_{act} of 0.47 eV, which is significantly lower than the E_{ads} of *OH (−2.87 eV) on Fe–N$_4$–C$_{64}$. The hydrogenation details (see Fig. 5f) indicate that the $d_{Fe–O}$ lengthens from 1.816 Å in IS6 to 2.010 Å in FS6, which indicates that the interaction between Fe–O is weakened, and the formed *H$_2$O can be easily detached from the Fe–N$_4$–C$_{64}$ surface due to its low E_{ads} of −0.75 eV. V_{freq} is i1298 cm^{-1} for TS5 and i1426 cm^{-1} for TS6, respectively. This describes the formation of *OH and the second *H$_2$O.

3.4.2 ORR mechanisms on Co–N$_4$–C$_{64}$. The ORR mechanisms on Co–N$_4$–C$_{64}$ were studied, and all conceivable pathways are shown in Fig. 6, where the red and blue lines represent the two pathways that facilitate the ORR on Co–N$_4$–C$_{64}$. The details of the ORR on Co–N$_4$–C$_{64}$ will be discussed next.

For O$_2$ chemisorbed on Co–N$_4$–C$_{64}$, there are two conceivable pathways: dissociation (*O$_2$ → *O + *O) and hydrogenation (*O$_2$ + *H → *OOH). For *O$_2$ → *O + *O, this reaction requires a large endothermic reaction energy of 1.46 eV and is accompanied by an insurmountable E_{act} of 2.93 eV, which means that the stage of *O$_2$ → *O + *O on Co–N$_4$–C$_{64}$ is extremely thermodynamically and kinetically disadvantageous. The

dissociation details are illustrated in Fig. 7a. Conversely, the hydrogenation of *O$_2$ to *OOH is more feasible because for *O$_2$ + *H → *OOH, this reaction has an exothermic reaction energy of 0.69 eV. Moreover, this process is accompanied by a very low E_{act} of 0.13 eV, which is evidently lower than the E_{ads} of *O$_2$ (−0.57 eV) on Co–N$_4$–C$_{64}$. The V_{freq} of TS8 is i981 cm^{-1}. The hydrogenation details (see Fig. 7b) indicate that $d_{O–H}$ decreases from 1.993 Å in IS8 to 1.356 Å in TS8 and to 0.982 Å in FS8. Meanwhile, $d_{Co–O}$ shortens from 1.859 Å in IS8 to 1.838 Å in FS8, and $d_{O–O}$ increases from 1.295 Å in IS8 to 1.416 Å in FS8. This implies that the interaction between Co–O is strengthened and that between O–O is weakened.

For the formed *OOH, there are two conceivable hydrogenation pathways: the *H attacks the O atom that bonds to Co to afford *H$_2$O$_2$ (*OOH + *H → *H$_2$O$_2$), or *H attacks the hydroxyl oxygen in *OOH to afford *O and *H$_2$O (*OOH + *H → *O + *H$_2$O).

For *OOH + *H → H$_2$O$_2$, this reaction has an exothermic reaction energy of 0.46 eV. Moreover, this process is accompanied by an E_{act} of 0.80 eV, which is obviously lower than the E_{ads} of *OOH (−1.54 eV) on Co–N$_4$–C$_{64}$. The hydrogenation details

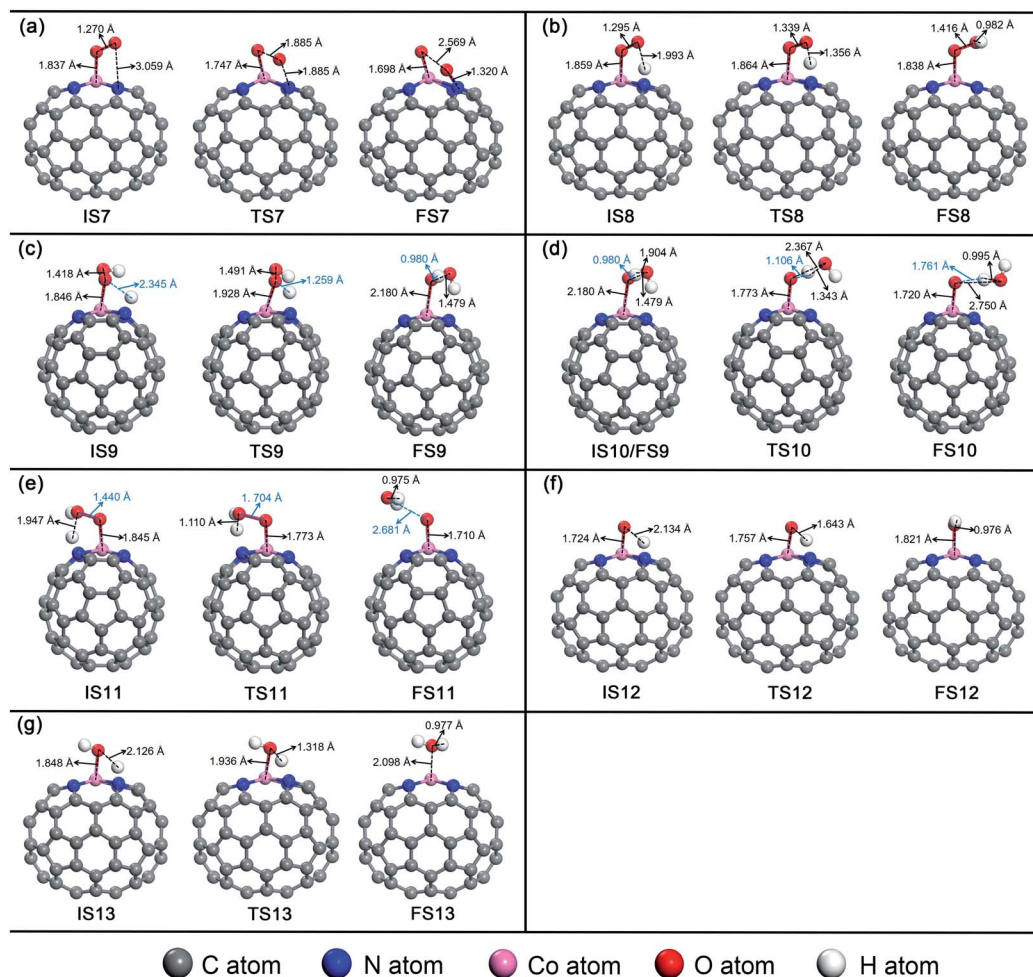**Fig. 7** The detailed process of the ORR on Co–N$_4$–C$_{64}$. (a) *O$_2$ → *O + *O, (b) *O$_2$ + *H → *OOH, (c) *OOH + *H → *H$_2$O$_2$, (d) *H$_2$O$_2$ → *O + *H$_2$O, (e) *OOH + *H → *O + *H$_2$O, (f) *O + *H → *OH, and (g) *OH + *H → *H$_2$O.

(see Fig. 7c) indicate that *H attacks the O atom that bonds to Co, and $d_{O–H}$ decreases from 2.345 Å in IS9 to 0.980 Å in FS9. Moreover, $d_{Co–O}$ increases from 1.846 Å in IS9 to 2.180 Å in FS9. The generated H_2O_2 is adsorbed on Co–N_4–C_{64} with an E_{ads} of −0.70 eV. Then, *H_2O_2 is instantly decomposed to *O + *H_2O because the reaction of *H_2O_2 → *O + *H_2O has an exothermic energy of 0.23 eV with a very low E_{act} of 0.33 eV, which means that the stage of *H_2O_2 → *O + *H_2O on Co–N_4–C_{64} is advantageous both thermodynamically and kinetically. Moreover, the energy required for this stage is lower than the E_{ads} of *H_2O_2 (−0.70 eV) on Co–N_4–C_{64}. It can be seen that although the *H_2O_2 on Co–N_4–C_{64} is formed by the 2e⁻ path, both thermodynamics and kinetics character enable its decomposition reaction to pass through the favorable 4e⁻ path again. The decomposition details (see Fig. 7d) indicate that the *H on the O atom that bonds to Co is transferred to the adjacent hydroxyl oxygen to generate the first *H_2O, and the generated *H_2O can be effortlessly separated from the Co–N_4–C_{64} surface, which only requires 0.43 eV. Meanwhile, $d_{Co–O}$ shortens from 2.180 Å in IS10/FS9 to 1.720 Å in FS10 and $d_{O–O}$ increases from 1.479 Å in IS10 to 2.750 Å in FS10, which implies that the interaction between Co–O is strengthened and the O–O bond is broken. The V_{freq} of i1469 cm⁻¹ for TS9 and i627 cm⁻¹ for TS10 respectively describe the formation and the decomposition of *H_2O_2.

For *OOH + *H → *O + *H_2O, this reaction has an exothermic reaction energy of 0.41 eV. Moreover, this process is accompanied by an E_{act} of 0.78 eV, which is obviously lower than the E_{ads} of *OOH (−1.54 eV) on Co–N_4–C_{64}. The V_{freq} of i768 cm⁻¹ in TS11 exactly exhibits the formation of *H_2O, and the formed *H_2O can easily detach from the Co–N_4–C_{64} surface, which only requires 0.26 eV. The hydrogenation details (see Fig. 7e) indicate that $d_{Co–O}$ shortens from 1.845 Å in IS11 to 1.710 Å in FS11 and that $d_{O–O}$ increases from 1.440 Å in IS11 to 2.681 Å in FS11; these findings respectively indicate that the interaction between Co–O is strengthened and the O–O bond is broken.

The above results manifest that for *OOH, regardless of whether it is first hydrogenated to form *H_2O_2 and then decomposed to *O + *H_2O or whether *OOH is directly hydrogenated to *O + *H_2O, it is conducive to ORR behavior on Co–N_4–C_{64}.

After the *H_2O is released, the atomic O remaining on Co experiences continuous hydrogenation to afford the second *H_2O: *O + *H → *OH and *OH + *H → *H_2O. The former reaction has a whopping exothermic reaction energy of 2.10 eV. Moreover, this process is accompanied by a very low E_{act} of 0.04 eV, which is significantly lower than the E_{ads} of *O (−2.62 eV) on Co–N_4–C_{64}. The hydrogenation details (see Fig. 7f) indicate that $d_{O–H}$ diminishes from 2.134 Å in IS12 to 0.976 Å in FS12. $d_{Co–O}$ lengthens from 1.724 Å in IS12 to 1.821 Å in FS12, which manifests that the interaction between Co–O is weakened with the formation of *OH. Then, the *OH remaining on Co experiences the succeeding hydrogenation: *OH + *H → *H_2O. This stage has an exothermic reaction energy of 0.86 eV. Moreover, this process is accompanied by a very low E_{act} of 0.22 eV, which is evidently lower than the E_{ads} of *OH (−2.54 eV) on Co–N_4–C_{64}. The hydrogenation details (see Fig. 7g) indicate

that $d_{Co–O}$ lengthens from 1.848 Å in IS13 to 2.098 Å in FS13; this indicates that the interaction between Co–O is weakened and the formed *H_2O can be effortlessly detached from the Co–N_4–C_{64} surface due to the low E_{ads} of −0.60 eV. The V_{freq} values of i918 cm⁻¹ for TS12 and i1467 cm⁻¹ for TS13 respectively describe the formation of *OH and the second *H_2O.

3.4.3 ORR mechanisms on Ni–N_4–C_{64}. The ORR mechanisms on Ni–N_4–C_{64} are also discussed. Firstly, the positive E_{ads} of 0.33 eV for *O_2 on Ni–N_4–C_{64} demonstrates that the ORR activity of Ni–N_4–C_{64} is unsatisfactory. Fig. 8 shows the 4e⁻ pathway through which the *O_2 on the Ni–N_4–C_{64} is hydrogenated to *OOH, then to *O + *H_2O; finally, the atomic O remaining on Ni is continuously hydrogenated. As can be viewed in Fig. 8, the stage of *OOH + *H → *O + *H_2O requires an endothermic reaction energy of 0.21 eV to complete. Moreover, the two stages for *O + *H → *OH and *OH + *H → *H_2O have extremely high energy barriers (3.25 eV and 2.97 eV). In conclusion, Ni–N_4–C_{64} is unfavorable as an ORR electrocatalyst.

3.5 PES and relative energy

The relative energy curve can be utilised as an effective method to assess the ORR properties of M–N_4–C_{64} (M = Fe, Co, and Ni). Fig. 9a–c exhibit the potential energy surface (PES) diagrams of Fe–N_4–C_{64}, Co–N_4–C_{64}, and Ni–N_4–C_{64}, correspondingly. In Fig. 9a and b, the green line denotes the stage of *O_2 → *O + *O. The blue line in Fig. 9a denotes the stage of *OOH + *H →
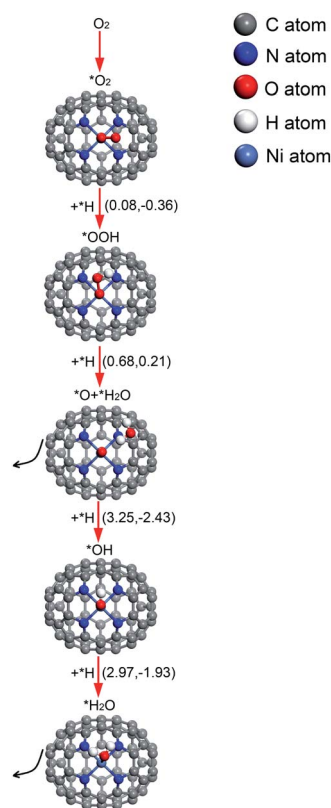

Fig. 8 The conceivable ORR pathway on Ni−N_4−C_{64}. The value on the left in parentheses is the activation energy and the value on the right is the reaction energy (in eV). * indicates adsorbed species.
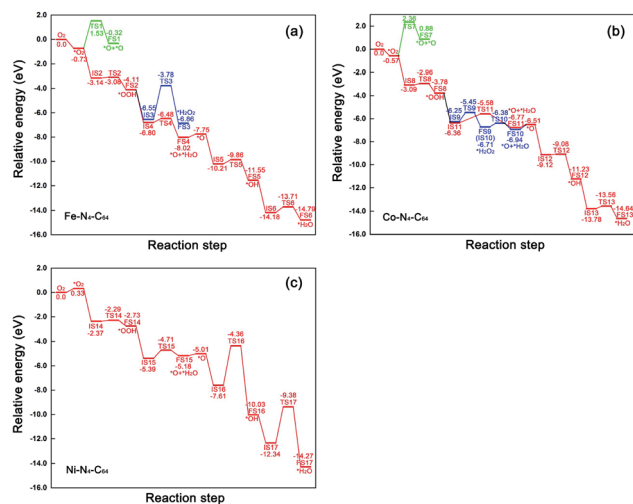
Fig. 9 Relative energy profiles of the conceivable ORR pathways on (a) Fe–N$_4$–C$_{64}$, (b) Co–N$_4$–C$_{64}$ and (c) Ni–N$_4$–C$_{64}$.

*H$_2$O$_2$ on Fe–N$_4$–C$_{64}$, and that in Fig. 9b denotes the two stages of *OOH + *H → *H$_2$O$_2$ and *H$_2$O$_2$ → *O + *H$_2$O on Co–N$_4$–C$_{64}$. For the red line path that can promote ORR on Fe–N$_4$–C$_{64}$ (see Fig. 9a), the first stage is to hydrogenate *O$_2$ to *OOH; *OOH is then hydrogenated to *O + *H$_2$O, and finally the atomic O remaining on Fe is continuously hydrogenated. The rate-limiting step (RLS) for the favorable red line path on Fe–N$_4$–C$_{64}$ is *OH + *H → *H$_2$O with an E_{act} of 0.47 eV. Moreover, the entire reaction energy variation of the red line path on Fe–N$_4$–C$_{64}$ is degressive, which is conducive to positive-going reactions. Co–N$_4$–C$_{64}$ can facilitate the ORR *via* two different paths (see Fig. 9b). One of the two paths is consistent with the aforementioned favorable ORR red line path on Fe–N$_4$–C$_{64}$. The RLS for this advantageous red line path on Co–N$_4$–C$_{64}$ is *OOH + *H → *O + *H$_2$O with an E_{act} of 0.78 eV. For the other path, the difference from the red line path is that the intermediate *OOH in this path is hydrogenated to *H$_2$O$_2$. The generated *H$_2$O$_2$ is immediately decomposed into *O + *H$_2$O to continue the 4e$^-$ path because this stage has an exothermic reaction energy of 0.23 eV with a much lower E_{act} (0.33 eV) than the E_{ads} of *H$_2$O$_2$ (−0.70 eV); finally, the atomic O remaining on Co is continuously hydrogenated. Moreover, the RLS for this feasible path on Co–N$_4$–C$_{64}$ is *OOH + *H → *H$_2$O$_2$ with an E_{act} of 0.80 eV. The entire reaction energy variation of the two favorable ORR paths on Co–N$_4$–C$_{64}$ is degressive, which is conducive to positive-going reactions. Meanwhile, Fig. 9c intuitively shows that Ni–N$_4$–C$_{64}$ as an ORR electrocatalyst is an unfavorable choice because the two stages for *O + *H → *OH and *OH + *H → *H$_2$O possess high energy barriers.

4. Conclusions

In this work, the density functional method was utilized to systematically study the co-doping of transition metal M and heteroatom N$_4$ in vacancy fullerene (M–N$_4$–C$_{64}$, M = Fe, Co, and Ni) as a novel type of non-precious ORR electrocatalyst. The

calculated formation energies indicated that Fe–N$_4$–C$_{64}$, Co–N$_4$–C$_{64}$ and Ni–N$_4$–C$_{64}$ are thermodynamically stable. Mulliken charge studies manifested that the metal center is the reaction site of the ORR and that the electron transfer from the metal center to N$_4$–C$_{64}$ is the largest in the Fe–N$_4$–C$_{64}$ system. PDOS revealed that the interaction between Fe–N$_4$–C$_{64}$ and the adsorbate is the strongest among the three, followed by Co–N$_4$–C$_{64}$ and finally Ni–N$_4$–C$_{64}$. The results of the calculated adsorption energies are consistent with the PDOS analysis. By analyzing and comparing the adsorption energies of the ORR species and the activation energies and reaction energies of all the basic ORR reaction steps involved in M–N$_4$–C$_{64}$, two favorable ORR electrocatalysts, Fe–N$_4$–C$_{64}$ and Co–N$_4$–C$_{64}$, were selected. Meanwhile, favorable ORR paths on Fe–N$_4$–C$_{64}$ and Co–N$_4$–C$_{64}$ were determined, and both catalysts used 4e$^-$ mechanisms to facilitate ORR. For Fe–N$_4$–C$_{64}$, the intermediate *OOH formed by hydrogenation of *O$_2$ on Fe–N$_4$–C$_{64}$ continues to be hydrogenated to *O + *H$_2$O, and finally, the *O remaining on Fe is continuously hydrogenated. The rate-limiting step (RLS) for the favorable path on Fe–N$_4$–C$_{64}$ is *OH + *H → *H$_2$O, with an E_{act} of 0.47 eV. For Co–N$_4$–C$_{64}$, the intermediate *OOH formed by hydrogenation of *O$_2$ on Co–N$_4$–C$_{64}$ can be directly hydrogenated to *O + *H$_2$O or firstly hydrogenated to *H$_2$O$_2$ and then promptly decomposes to *O + *H$_2$O; finally, the *O remaining on Co is continuously hydrogenated. The RLS of the two advantageous paths on Co–N$_4$–C$_{64}$ is the hydrogenation stage of the intermediate *OOH, and the corresponding activation energies are 0.78 eV for *OOH + *H → *O + *H$_2$O and 0.80 eV for *OOH + *H → *H$_2$O$_2$, correspondingly. PES diagrams intuitively reflect that the whole reaction energy variation in the favorable ORR paths of Fe–N$_4$–C$_{64}$ and Co–N$_4$–C$_{64}$ is degressive, which is conducive to positive-going reactions. This study demonstrates that Fe–N$_4$–C$_{64}$ and Co–N$_4$–C$_{64}$ are high-efficiency ORR electrocatalysts. We expect that the proposed transition metal and heteroatom N$_4$ co-doped in vacancy fullerene can contribute to the development of cathode materials for FCs.

Conflicts of interest

There are no conflicts to declare.

Acknowledgements

References

1 Y. Wang, K. S. Chen, J. Mishler, S. C. Cho and X. C. Adroher, *Appl. Energy*, 2011, **88**, 981–1007.
2 S. Sui, X. Wang, X. Zhou, Y. Su, S. B. Riffat and C. Liu, *J. Mater. Chem.*, 2017, **5**, 1808–1825.
3 S. Wang and S. P. Jiang, *Natl. Sci. Rev.*, 2017, **4**, 163–166.

4 E. H. Majlan, D. Rohendi, W. R. W. Daud, T. Husaini and M. A. Haque, *Renew. Sust. Energ. Rev.*, 2018, **89**, 117–134.

5 K. Gong, F. Du, Z. Xia, M. F. Durstock and L. Dai, *Science*, 2009, **323**, 760–764.

6 Y. Jiao, Y. Zheng, M. Jaroniec and S. Qiao, *Chem. Soc. Rev.*, 2015, **44**, 2060–2086.

7 C. Zhu, H. Li, S. Fu, D. Du and Y. Lin, *Chem. Soc. Rev.*, 2016, **45**, 517–531.

8 C. Zhu, S. Fu, Q. Shi, D. Du and Y. Lin, *Angew. Chem., Int. Ed.*, 2017, **56**, 13944–13960.

9 H. A. Gasteiger, S. S. Kocha, B. Sompalli and F. T. Wagner, *Appl. Catal. B-Environ.*, 2005, **56**, 9–35.

10 Y. Zheng, D. Yang, J. M. Kweun, C. Li, K. Tan, F. Kong, C. Liang, Y. J. Chabal, Y. Y. Kim and M. Cho, *Nano Energy*, 2016, **30**, 443–449.

11 Z. Liang, H. Zheng and R. Cao, *Sustain. Energy Fuels*, 2020, **4**, 3848–3870.

12 M. K. Debe, *Nature*, 2012, **486**, 43–51.

13 J. Liu, M. Jiao, B. Mei, Y. Tong, Y. Li, M. Ruan, P. Song, G. Sun, L. Jiang and Y. Wang, *Angew. Chem., Int. Ed.*, 2019, **58**, 1163–1167.

14 L. Liu, G. Zeng, J. Chen, L. Bi, L. Dai and Z. Wen, *Nano Energy*, 2018, **49**, 393–402.

15 X. Ren, Q. Lv, L. Liu, B. Liu, Y. Wang, A. Liu and G. Wu, *Sustain. Energy Fuels*, 2020, **4**, 15–30.

16 J. Kim, H. Kim and H. Lee, *Chemsuschem*, 2018, **11**, 104–113.

17 B. Lu, Q. Liu and S. Chen, *ACS Catal.*, 2020, **10**, 7584–7618.

18 H. Fei, J. Dong, M. J. Arellanojimenez, G. Ye, N. D. Kim, E. L. G. Samuel, Z. Peng, Z. Zhu, F. Qin and J. Bao, *Nat. Commun.*, 2015, **6**, 8668.

19 H. J. Qiu, Y. Ito, W. Cong, Y. Tan, P. Liu, A. Hirata, T. Fujita, Z. Tang and M. Chen, *Angew. Chem., Int. Ed.*, 2015, **54**, 14031–14035.

20 C. Zhao, X. Dai, T. Yao, W. Chen, X. Wang, J. Wang, J. Yang, S. Wei, Y. Wu and Y. Li, *J. Am. Chem. Soc.*, 2017, **139**, 8078–8081.

21 X. Wang, Z. Chen, X. Zhao, T. Yao, W. Chen, R. You, C. Zhao, G. Wu, J. Wang and W. Huang, *Angew. Chem., Int. Ed.*, 2018, **57**, 1944–1948.

22 P. Chen, T. Zhou, L. Xing, K. Xu, Y. Tong, H. Xie, L. Zhang, W. Yan, W. Chu and C. Wu, *Angew. Chem., Int. Ed.*, 2017, **56**, 610–614.

23 M. Xiao, J. Zhu, L. Ma, Z. Jin, J. Ge, X. Deng, Y. Hou, Q. He, J. Li, Q. Jia, S. Mukerjee, R. Yang, Z. Jiang, D. Su, C. Liu and W. Xing, *ACS Catal.*, 2018, **8**, 2824–2832.

24 X. Yang, A. Wang, B. Qiao, J. Li, J. Liu and T. Zhang, *Acc. Chem. Res.*, 2013, **46**, 1740–1748.

25 T. Xu, W. Shen, W. Huang and X. Lu, *Mater. Today Nano*, 2020, **11**, 100081.

26 K. Minami, Y. Kasuya, T. Yamazaki, Q. Ji, W. Nakanishi, J. P. Hill, H. Sakai and K. Ariga, *Adv. Mater.*, 2015, **27**, 4020–4026.

27 Z. Tan, K. Ni, G. Chen, W. Zeng, Z. Tao, M. Ikram, Q. Zhang, H. Wang, L. Sun and X. Zhu, *Adv. Mater.*, 2017, **29**, 1603414.

28 L. Rincongarcia, A. K. Ismael, C. Evangeli, I. Grace, G. Rubiobollinger, K. Porfyrakis, N. Agrait and C. J. Lambert, *Nat. Mater.*, 2016, **15**, 289–293.

29 K. Liu, S. Gao, Z. Zheng, X. Deng, S. Mukherjee, S. Wang, H. Xu, J. Wang, J. Liu, T. Zhai and Y. Fang, *Adv. Mater.*, 2019, **31**, e1808254.

30 J. M. Hawkins, A. Meyer and M. A. Solow, *J. Am. Chem. Soc.*, 1993, **115**, 7499–7500.

31 K. Choho, W. Langenaeker, G. V. De Woude and P. Geerlings, *J. Mol. Struct.*, 1995, **338**, 293–301.

32 M. R. Benzigar, S. Joseph, H. Ilbeygi, D. Park, S. Sarkar, G. K. Chandra, S. Umapathy, S. Srinivasan, S. N. Talapaneni and A. Vinu, *Angew. Chem., Int. Ed.*, 2018, **57**, 569–573.

33 M. R. Benzigar, S. Joseph, A. V. Baskar, D. Park, G. K. Chandra, S. Umapathy, S. N. Talapaneni and A. Vinu, *Adv. Funct. Mater.*, 2018, **28**, 1803701.

34 Y. Lin and D. S. Su, *ACS Nano*, 2014, **8**, 7823–7833.

35 S. Gao, X. Wei, H. Fan, L. Li, K. Geng and J. Wang, *Nano Energy*, 2015, **13**, 518–526.

36 X. Chen, J. Chang and Q. Ke, *Carbon*, 2018, **126**, 53–57.

37 Y. Wang, M. Jiao, W. Song and Z. Wu, *Carbon*, 2017, **114**, 393–401.

38 F. Banhart, J. Kotakoski and A. V. Krasheninnikov, *ACS Nano*, 2011, **5**, 26–41.

39 Y. Chen, S. Ji, S. Chen, Q. Peng, D. Wang and Y. Li, *Joule*, 2018, **2**, 1242–1264.

40 D. H. Lee, W. J. Lee, W. J. Lee, S. O. Kim and Y.-H. Kim, *Phys. Rev. Lett.*, 2011, **106**, 175502.

41 H. Fei, J. Dong, Y. Feng, C. S. Allen, C. Wan, B. Volosskiy, M. Li, Z. Zhao, Y. Wang, H. Sun, P. An, W. Chen, Z. Guo, C. Lee, D. Chen, I. Shakir, M. Liu, T. Hu, Y. Li, A. I. Kirkland, X. Duan and Y. Huang, *Nat. Catal.*, 2018, **1**, 63–72.

42 Y. Chen, S. Ji, Y. Wang, J. Dong, W. Chen, Z. Li, R. Shen, L. Zheng, Z. Zhuang and D. Wang, *Angew. Chem., Int. Ed.*, 2017, **56**, 6937–6941.

43 X. Li, S. Xi, L. Sun, S. Dou, Z. Huang, T. Su and X. Wang, *Adv. Sci.*, 2020, **7**, 2001545.

44 F. Callevallejo, J. I. Martinez and J. Rossmeisl, *Phys. Chem. Chem. Phys.*, 2011, **13**, 15639–15643.

45 S. Kattel and G. Wang, *J. Mater. Chem.*, 2013, **1**, 10790–10797.

46 S. Kattel and G. Wang, *J. Phys. Chem. Lett.*, 2014, **5**, 452–456.

47 X. Chen, R. Hu and F. Bai, *Materials*, 2017, **10**, 549.

48 B. Modak, K. Srinivasu and S. K. Ghosh, *Int. J. Hydrogen Energy*, 2017, **42**, 2278–2287.

49 B. Delley, *J. Chem. Phys.*, 2000, **113**, 7756–7764.

50 J. P. Perdew, K. Burke and M. Ernzerhof, *Phys. Rev. Lett.*, 1996, **77**, 3865–3868.

51 K. Liu, S. Kattel, V. Mao and G. Wang, *J. Phys. Chem. C*, 2016, **120**, 1586–1596.